Evaluation of a regularized SAR imaging technique based on recognition-oriented features

Müjdat Çetin, W. Clem Karl, and David A. Castañon

Multi-Dimensional Signal Processing Laboratory, Dept. of ECE
Boston University, 8 Saint Mary's Street, Boston, MA 02215, USA

ABSTRACT

One of the biggest challenges for automatic target recognition (ATR) methods is the accurate and efficient extraction of features from synthetic aperture radar (SAR) images. We have recently developed a new SAR image formation technique which is recognition-oriented in the sense that it enhances features in the scene which we believe are important for recognition purposes. In this paper, we evaluate the performance of the images produced by this technique in terms of preserving and enhancing these features. The findings of our analysis indicate that the new SAR image formation method provides images with higher resolution of scatterers, and better separability of different regions as compared to conventional SAR images.

Keywords: Synthetic aperture radar, image reconstruction, non-quadratic regularization, feature extraction, super-resolution, segmentation, automatic target recognition

1. INTRODUCTION

Automatic target recognition (ATR) methods based on synthetic aperture radar (SAR) imagery need to extract certain features from the reconstructed images. Such robust feature extraction can be difficult when based on SAR images formed by conventional methods, such as the polar format algorithm.[1] One challenge is that the resolution of the formed images is limited by the SAR system bandwidth. This complicates point scatterer localization. In addition, the images suffer from speckle. This complicates region segmentation for shape-based recognition.

We have recently developed an alternative SAR image formation method, based on non-quadratic regularization.[2] This method produces images which appear to enhance point-based features (e.g. scatterer locations), and region-based features (e.g. object shapes). Such features are important for recognition purposes.[3–6]

In this paper, we propose quantitative criteria for evaluating the images produced by this new regularized SAR image formation technique. We run experiments on the Moving and Stationary Target Acquisition and Recognition (MSTAR) public target data set to compare the SAR images formed by the regularized method to conventional images in terms of these quantitative measures. The criteria we use regarding point-based features are target-to-clutter ratio, main-lobe width, peak matching accuracy, and average associated peak distance. The metric of peak matching accuracy is particularly useful for testing the superresolution properties of an image formation method. The criteria we use for region-based features are speckle suppression, segmentation accuracy, and separability of different regions models.

The results of this study show that emphasizing point-based features through the new image formation method yields images with higher resolution and better dominant scatterer localization than conventional images. Our experiments indicate that the method is able to produce accurate superresolution reconstructions from considerably reduced amounts of data. Emphasizing region-based features on the other hand, results in enhanced anomaly and speckle suppression in homogeneous regions, and hence, easier-to-segment images. Our results should be compared to those in similar analyses carried out for other enhanced SAR image formation techniques.[7–9]

Further author information: (Send correspondence to M.Ç.)
M.Ç.: E-mail: mcetin@bu.edu
W.C.K.: E-mail: wckarl@bu.edu
D.A.C.: E-mail: dac@bu.edu

2. SAR IMAGE FORMATION BASED ON NON-QUADRATIC REGULARIZATION

We will provide a brief overview of our image formation scheme, the details of which can be found in Ref. 2. We start from the following assumed discrete model for the SAR observation process:

$$g = Tf + w, \tag{1}$$

where g are the SAR observations (phase histories or range profiles), f is the unknown sampled reflectivity image, w is additive measurement noise, all column stacked as vectors, and T is a complex-valued SAR observation matrix. If phase history data are used, T is a 2-D Fourier-type operator,[10] and if range profile data are used, T is a complex-valued projection-type operator. In this framework, the objective of SAR image reconstruction is to obtain an estimate of f based on the data g. The conventional SAR polar format image formation algorithm can roughly be interpreted in this framework as the application of the adjoint to the data: $\hat{f} = T^H g$.

In contrast, we formulate the SAR image reconstruction problem as an optimization problem of the following form:

$$\hat{f} = \arg\min_f \left[\|g - Tf\|_2^2 + \lambda_1^2 \|f\|_k^k + \lambda_2^2 \||D|f|\|_k^k \right] \tag{2}$$

where $\| \cdot \|_p$ denotes the ℓ_p norm, and D is a 2-D derivative operator. We consider values of k near 1. The first term in the above objective function is a data fidelity term. The other two terms reflect the prior information concerning the behavior of f that we would like to impose.

Use of non-quadratic constraints, such as those in Eq. 2, has recently become popular, e.g. in image restoration,[11] due to the ability of these constraints to prevent suppression of useful features in the image. The objective function in Eq. (2) extends the use of such constraints to the complex-valued SAR image reconstruction problem.

Since SAR object recognition methods usually rely on dominant point scatterer locations and/or object shapes, we use an explicit prior term in Eq. (2) for each type of feature. The term $\|f\|_k^k$ is an energy-type constraint on the solution, and aims to suppress artifacts and increase the resolvability of point scatterers. The $\||D|f|\|_k^k$ term on the other hand, aims to reduce variability in homogeneous regions. The relative magnitudes of λ_1 and λ_2 determine the emphasis on point-based versus region-based features. Therefore, this framework lets us reconstruct images with two different flavors: using a relatively large λ_1 yields point-enhanced imagery, and using a relatively large λ_2 yields region-enhanced imagery. We solve the optimization problem in Eq. (2) using an efficient iterative algorithm we have developed in Ref. 2, based on half-quadratic regularization.[12]

3. FEATURE-BASED CRITERIA FOR EVALUATION OF IMAGE QUALITY

In this section we propose measures for evaluating the quality of images formed by the method outlined in Sect. 2. Many of these criteria have appeared in the literature before, and they are mostly directed towards images to be used in target recognition tasks.

3.1. Criteria for Point-Enhanced Images

3.1.1. Target-to-clutter ratio

As a measure of accentuation of the target pixels with respect to the background, we will use the target-to-clutter ratio in dB, defined as[9]:

$$\text{Target−to−clutter ratio} = 20 \log_{10} \left(\frac{\max(|\hat{f}(i,j)|)}{\frac{1}{N_{\mathcal{C}}} \sum_{(i,j) \in \mathcal{C}} |\hat{f}(i,j)|} \right) \tag{3}$$

where $\hat{f}(i,j)$ is the reconstructed image, with the pair (i,j) denoting the pixel indices, $\mathcal{C}$ denotes a clutter patch in the image, and $N_{\mathcal{C}}$ denotes the number of pixels in that patch.

3.1.2. Main-lobe width

As one of the measures of the effective resolution of an image, we will use the 3-dB main-lobe width. To obtain an estimate of the main-lobe width, we concentrate on the target region. In each row and column in the target region of the reconstructed image, we find the first point near the maximum where the reflectivity magnitude is more than 3 dB below the maximum value. We then obtain a better estimate of the 3-dB distance by means of a linear interpolation between pixels. Finally, we average the distances obtained from each row and column in the target region to find an overall estimate of the 3-dB lobe width for a particular image.

3.1.3. Peak matching accuracy

Locations of dominant point scatterers extracted from a target image are important characteristics for recognition.[3,4] Loss of resolution manifests itself by merging and moving such characteristic points, and this makes the accurate localization of these points in the scene more difficult. Thus, we evaluate the superresolution properties of our method by measuring how well the dominant scatterers are preserved when we use reduced-resolution data to form the image.

For this purpose, we extract the locations of the 20 brightest scatterers from the conventional and the proposed reconstructions using the same reduced-resolution data, and compare these to the "reference" locations of the scatterers. These "reference" positions may be obtained either from the ground truth, in case that is available, or from the locations of the scatterers extracted from a higher resolution image otherwise.

In order to extract the scatterer locations, we first find the peaks in the reconstructed image. The peaks are taken to be the points where the discrete spatial derivatives of the reflectivity magnitude in both the x and the y directions change sign from positive to negative. Once the peaks are found, we order them based on their magnitude, and pick the largest 20.

Once the peaks are extracted, we evaluate how well the coordinates of these 20 peaks match those of the 20 "reference" peaks. For this task, we use the peak matching method also used in Ref. 13. This method allows a match declaration between two peaks, if the estimated peak location is within a radius r of the "reference" peak location. Hence it is more powerful than counting only the exact matches, with r used as a variable parameter ($r = 0$ corresponds to counting the exact matches). A one-to-one association of the peaks is made such that the sum of the squared distances between the locations of the "reference" peaks and the corresponding matched peaks from the image is minimized. We can then count the number of matched peaks out of 20, to see how well the peaks are preserved.

3.1.4. Average associated peak distance

Another criterion based on peak locations that we will use is the average distance between the two sets of 20 peak coordinates. To compute this measure, we relax the matching radius r of Sect. 3.1.3, so that each of the 20 peaks from the reconstructed image are matched to a "reference" peak. We then find the average of the distances between these associated peaks.

3.2. Criteria for Region-Enhanced Images

3.2.1. Speckle suppression

Speckle complicates intensity-based region description in conventional SAR images. One measure that has been used for speckle amplitude is the standard deviation of a clutter patch in the dB-valued SAR images.[9] We use this measure to quantitatively compare our reconstructions with conventional images in terms of speckle suppression.

3.2.2. Segmentation accuracy

It is of interest to obtain accurate segmentations of SAR images for effective use of region-based shape features in target recognition. Recently there has been much interest in the development of segmentation algorithms for conventional SAR images. Our region-enhanced images provide easier-to-segment regions as compared to conventional SAR images. We will demonstrate this property by segmenting our reconstructions to target, shadow and background regions by simple adaptive thresholding. To determine the threshold, we find the mean μ and the standard deviation σ of the dB-valued pixel magnitudes in the image. Then, we apply the following decision rule at each pixel:

$$20 \log_{10}(\hat{f}(i,j)) < \mu - c_1\sigma \quad\quad \implies \quad \hat{f}(i,j) \in \mathcal{S}$$
$$\mu - c_1\sigma \leq 20 \log_{10}(\hat{f}(i,j)) < \mu + c_2\sigma \quad \implies \quad \hat{f}(i,j) \in \mathcal{B}$$
$$\mu + c_2\sigma \leq 20 \log_{10}(\hat{f}(i,j)) \quad\quad \implies \quad \hat{f}(i,j) \in \mathcal{T}$$

where $\mathcal{T}, \mathcal{S}, \mathcal{B}$ denote the target, shadow and background regions respectively and c_1, c_2 are two constants that are fixed beforehand.

From a statistical standpoint, it would make more sense to develop a decision metric based on statistics of particular regions. However, our objective here is not to develop the best decision metric, but rather to show that we can obtain reasonable segmentations of the region-enhanced images even by simple suboptimal processing.

3.2.3. Region histograms

In order to observe the class separability properties of the reconstructed images, we will present the histograms of the target, shadow, and background regions in the reconstructed images.

4. EXPERIMENTAL RESULTS

4.1. Experimental Setup

We use images of T72 (*sn_132*) tanks, BMP2 (*sn_c21*) tanks, and BTR70 (*sn_c71*) armored personnel carriers from the MSTAR public target data set to evaluate the performance of our reconstructed images in terms of the criteria described in Sect. 3. We use 72 images for each vehicle type, all at 17° depression angle, and evenly spaced in azimuth (approximately 5°) to cover 360°. Figure 1 shows the magnitude of an example MSTAR image in dB for each target type. We will use these three images to display the nature of our reconstructions and the associated feature extraction results. As we will describe, we also carry out some synthetic scene reconstruction experiments to make some evaluations where ground truth is exactly known.

In order to apply our algorithm, we need the phase histories (or the range profiles). We obtain the phase histories from the 128×128 complex-valued MSTAR images, by undoing the final steps of MSTAR image formation, as done in Ref. 7. We first take the 2-D Discrete Fourier Transform (DFT) of the images, then we remove the zero-padding to obtain 100×100 phase history samples. Next we remove the windowing applied. From the MSTAR file headers, we know that a 35 dB Taylor window has been used, and we assume that the order of the Taylor window used is $\overline{n} = 4$. We divide the phase history samples by a 2-D Taylor window we thus obtain.

When applying our image reconstruction method, we choose the feature accentuation parameters λ_1 and λ_2 in Eq. (2) based on subjective qualitative assessment of one image from the entire data set, and use those values for all the images for that particular experiment. Of course, this choice is coupled with our imaging goals, that is, a relatively large value of λ_1 is used for point-based feature enhancement, and a relatively large value of λ_2 is used for region-based feature enhancement.

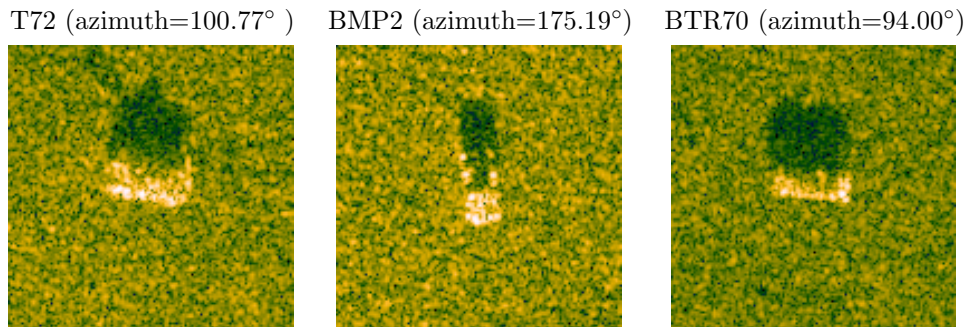T72 (azimuth=100.77°)   BMP2 (azimuth=175.19°)   BTR70 (azimuth=94.00°)

Figure 1. Sample images from the MSTAR public target data set.

4.2. Point-Enhanced Imaging from Full-Resolution Data

We now use the 100×100 phase history samples to form point-enhanced images. We will form "critically-sampled" (i.e. 100×100) images. Therefore, in order to have conventional SAR images of this size for comparison, we first form 100×100 Taylor-windowed Fourier images. Samples of such reconstructions are shown in the top row of Fig. 2. Naturally these are very similar to their oversampled versions in Fig. 1.

We form point-enhanced images with $k = 0.8$, and $\lambda_2 = 0$ in Eq. (2). We do not apply any windowing to the data before processing, since our method is able to suppress sidelobes considerably even with rectangular weighting. However, if desired, the method can be used with windowing. The bottom row in Fig. 2 shows the reconstructions obtained. The dominant scatterers appear to be accentuated as compared to the conventional images at the top row.
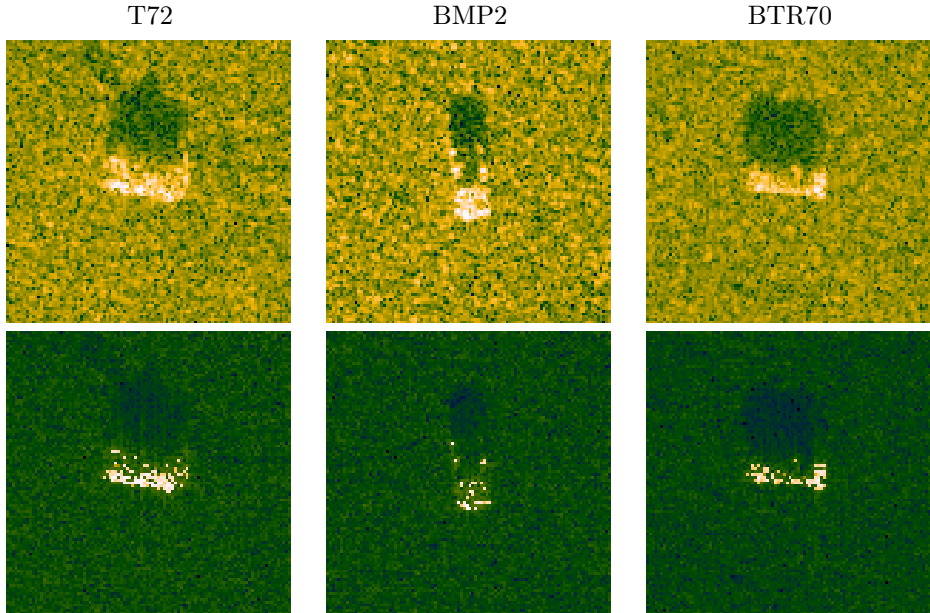

Figure 2. Sample images reconstructed from full-resolution (100×100) data. Top: conventional. Bottom: proposed point-enhanced.

4.2.1. Target-to-clutter ratio

We will quantify the enhancement of the target pixels in the full-resolution data reconstructions by means of their target-to-clutter ratio. We compute the target-to-clutter ratio as defined in Eq. (3), by using the bottom 20 rows (2000 pixels) of the reconstructed images as the clutter region. This region is big enough to give a reliable estimate of the mean reflectivity magnitude, and is safe to use, since target and shadow appear to be located outside this region for the entire data set. Table 1 shows the average target-to-clutter ratio achieved by the conventional and the proposed methods over the 72 reconstructed images for each target type. These results indicate a clear improvement of the target-to-clutter ratio by our proposed image formation method.

Average Target-to-Clutter Ratio	T72	BMP2	BTR70
Conventional	31.88 dB	28.92 dB	26.92 dB
Proposed	88.28 dB	85.38 dB	82.62 dB

Table 1. Average target-to-clutter ratios of images reconstructed from full-resolution data.

4.3. Point-Enhanced Superresolution Imaging from Reduced-Resolution Data

In this section, we carry out experiments on two sets of data: those from the actual MSTAR images, and those from synthetic point scatterer scenes constructed using the MSTAR images. The reason for using synthetic examples is to

demonstrate the superresolution properties of our method in a situation where the ground truth is exactly known.

We will present the main-lobe width results for the actual MSTAR reconstructions only. We will present the peak matching accuracy and the average associated peak distance results for both actual and synthetic images. We do not present the target-to-clutter ratio results in this section, since they are very similar to the full-resolution target-to-clutter ratio results of Table 1.

For experiments on actual MSTAR data, we form images from a 50×50 subset of the 100×100 phase history samples previously used. This results in a two times resolution loss in the range and cross-range directions. All the images we will form in this section are composed of 100×100 pixels. The top row in Fig. 3 shows Taylor weighted Fourier images from these reduced-resolution data. The resolution loss in these images is evident when they are compared to their high-resolution counterparts in Fig. 2. We now form point-enhanced images with $k = 0.8$, and $\lambda_2 = 0$ in Eq. (2), samples of which are shown in the bottom row of Fig. 3.
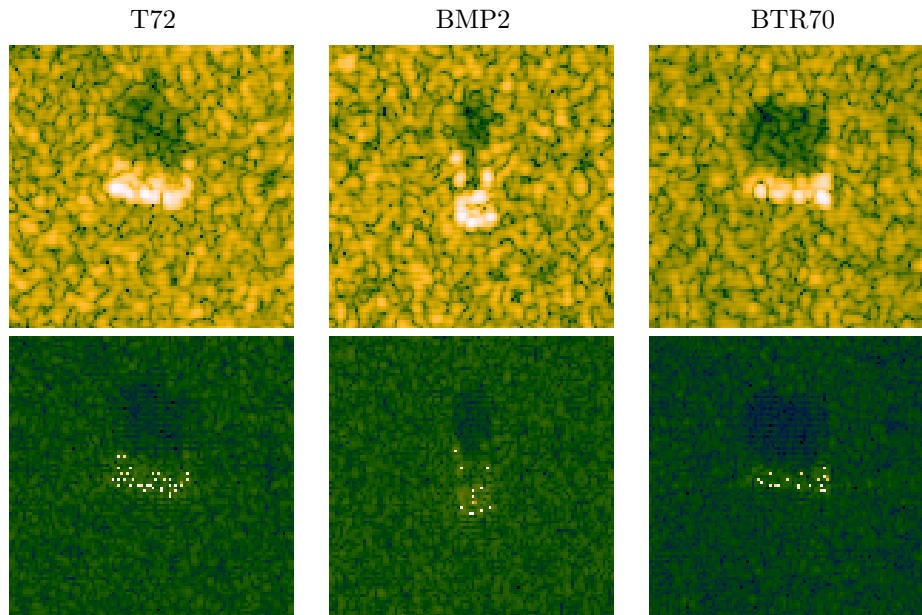

Figure 3. Sample images reconstructed from reduced-resolution (50×50) data. Top: conventional. Bottom: proposed point-enhanced.

We now consider the synthetic examples. To generate synthetic scenes we find the 20 peaks with the largest magnitude in each of the 72 100×100 Taylor-windowed T72 Fourier images, and form a synthetic scene by placing simulated point-scatterers at the locations of these peaks, with the original complex reflectivities, and zeros in the rest of the scene. An example contour plot of the magnitude of such a synthetic scene is shown in the left third of Fig. 4. We then generate simulated phase histories from this scene. The reconstructed conventional Taylor-windowed image from 50×50 phase history samples is shown at the top row, middle column of Fig. 4. The loss of resolution is easy to observe. The corresponding point-enhanced image produced by our method is shown at the bottom row, middle column of the same figure, and we can visually observe that most of the scatterers that were merged by the conventional reconstruction are now resolved. The images in the rightmost column demonstrate similar results for the 25×25 data case. Although the amount of data we use here is only one sixteenth of the data required for full resolution, our method is able to localize most of the scatterers.

In the remainder of this section, we will quantitatively demonstrate the resolution improvement achieved by the images presented here.

4.3.1. Main-lobe width

We compute the average 3-dB main-lobe width as described in Sect. 3.1.2 for all the 216 reconstructed MSTAR scenes. The results in Table 2 for 50×50 data reconstructions show that our proposed scheme is able to reduce
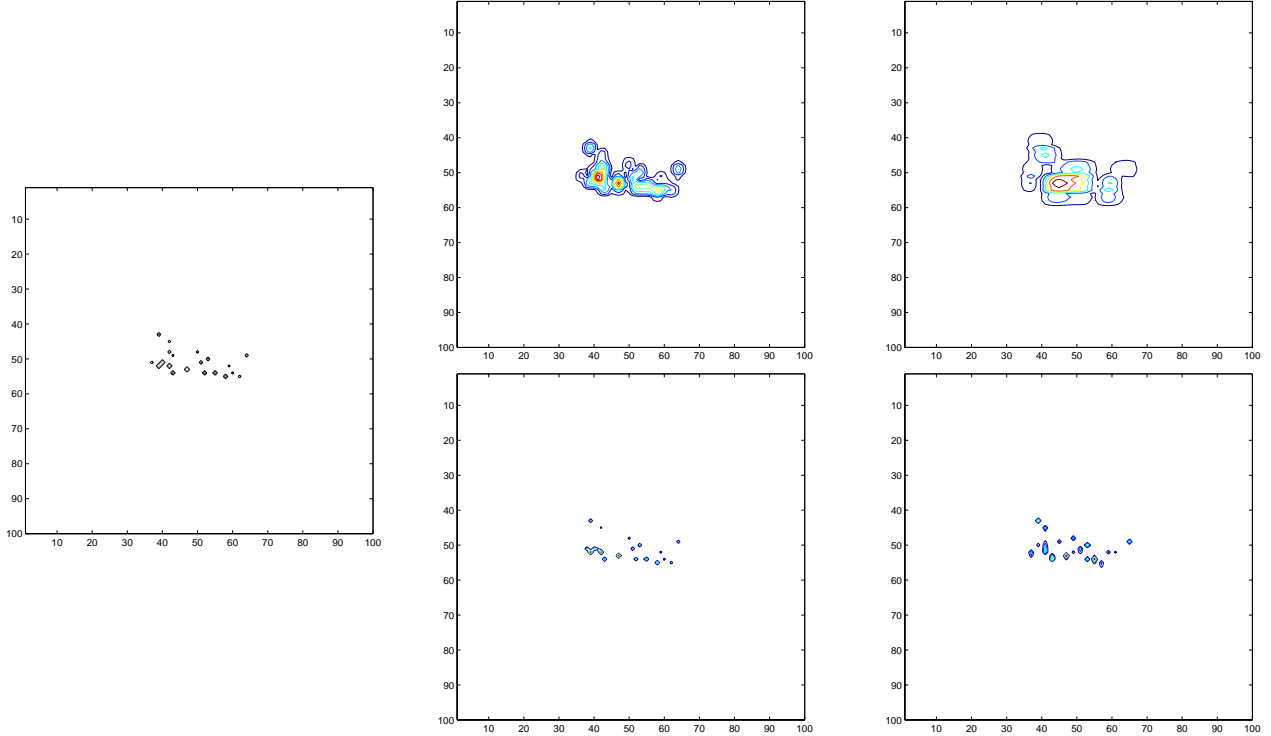
Figure 4. Synthetic T72 image reconstruction example from reduced-resolution data. Left: ground truth. Middle: results from 50×50 data. Right: results from 25×25 data. Top row: conventional. Bottom row: proposed point-enhanced.

the lobe width considerably. To put these numbers in perspective, note that the resolution supported by the data is 0.6 m in this experiment.

Average Main-Lobe Width	T72	BMP2	BTR70
Conventional	0.447 m.	0.466 m.	0.459 m.
Proposed	0.098 m.	0.097 m.	0.094 m.

Table 2. Average main-lobe widths of images reconstructed from reduced-resolution (50×50) data.

4.3.2. Peak matching accuracy

We now evaluate how the locations of the dominant peaks are preserved in reduced-resolution data situations by the conventional reconstructions and by our point-enhanced images. For the MSTAR examples, we use the locations of the 20 peaks extracted from the Taylor-windowed image reconstructed from full data, as the "reference" locations. Fig. 5 provides a visual comparison of the peak locating accuracy of the reconstructions from 50×50 data. The circles indicate the "reference" locations of the 20 dominant scatterers, and the plus signs indicate the peaks extracted from the reconstructed reduced-resolution images. The top row contains the results for the conventional images, while the bottom row contains those for the point-enhanced images. The clear observation we can make out of these results is that, since conventional image formation causes peaks to merge, some of the peaks in the target area are lost, and peaks outside this area may become dominant. We will now evaluate the peak matching accuracy of our method by using the criterion described in Sect. 3.1.3. In Fig. 6, we plot the average number of peak matches for the images formed by the conventional and the proposed methods as a function of the radius r within which a match declaration is allowed. The standard deviation of this estimate of the mean is small enough, hence we do not show error bars on these plots. The peak matching accuracy of our images appear to be higher than that of the the conventional images. Note that our analysis is based on finding peaks all around the scene. Alternatively, the search for peaks can be done in a pre-determined target region only.
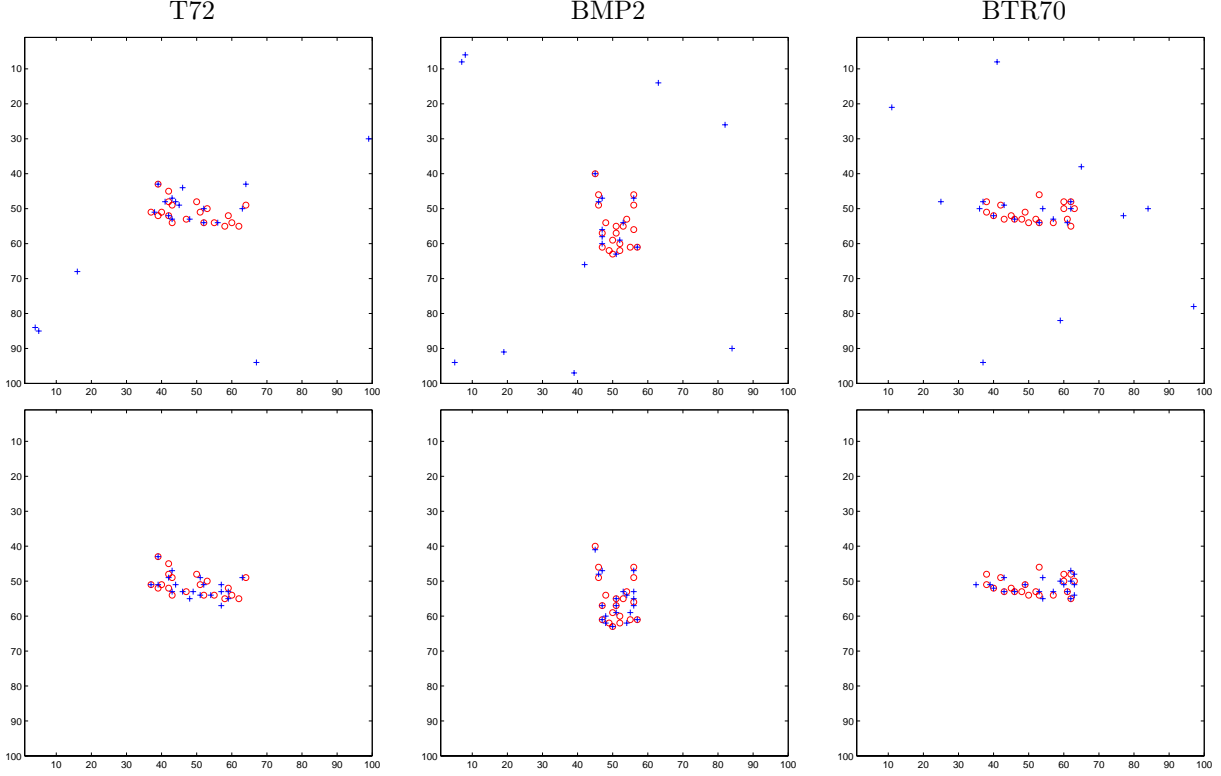
Figure 5. Sample peak extraction results for images reconstructed from 50×50 data. Circles indicate "reference" dominant scatterer locations extracted from full-resolution Taylor Fourier images. Plus signs indicate peaks extracted from the reconstructed images. Top: conventional. Bottom: proposed point-based.
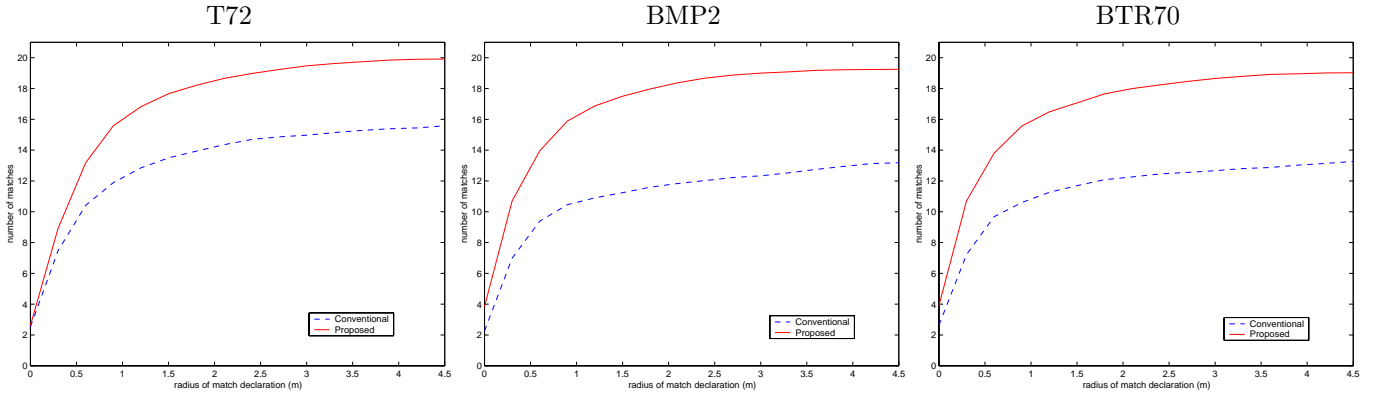

Figure 6. Average number of peak matches in images reconstructed from reduced-resolution (50×50) data as a function of the radius of match declaration r.

We now carry out similar experiments for the synthetic T72 scenes. Fig. 7 compares peaks extracted from our images with those from the conventional ones using 50×50 and 25×25 data. The improved accuracy provided by our method is easy to observe in these plots. Similarly, the peak matching results from the entire data, shown in Fig. 8, verify the superresolution properties of our imaging scheme.

4.3.3. Average associated peak distance

We now compute the average distance between the true 20 peaks and the 20 peaks extracted from the reconstructed images as described in Sect. 3.1.4. Tables 3 and 4 illustrate the average associated peak distances for the actual and synthetic scene experiments respectively. These results indicate a clear reduction in peak distances by our method.
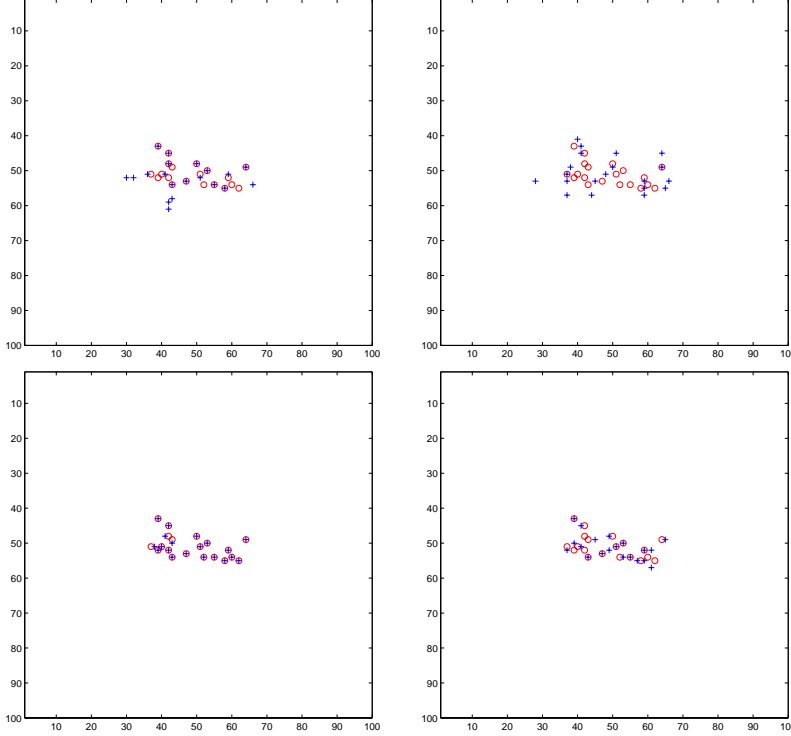
Figure 7. Sample peak extraction results for the synthetic T72 scenes. Circles indicate the scatterer locations in the synthetic scene. Plus signs indicate peaks extracted from the reconstructed images. Left: 50×50 data. Right: 25×25 data. Top: conventional. Bottom: proposed point-based.

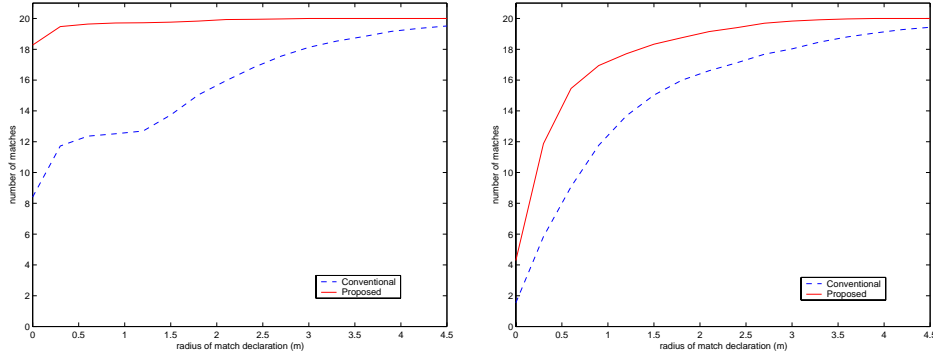**Figure 8.** Average number of peak matches for the synthetic T72 scenes as a function of the radius of match declaration r. Left: 50×50 data. Right: 25×25 data.

4.4. Region-Enhanced Imaging

We now compare our region-enhanced images with conventional ones in terms of the criteria described in Sect. 3.2. Here, we form 128×128 images from 128×128 Taylor-weighted phase history samples. In our image reconstruction method, we use $k = 1$, and set $\lambda_2 > \lambda_1$ in Eq. (2) to enhance regions. The second row of Fig. 9 shows sample reconstructions using the proposed method. In contrast to the conventional images in the top row, these reconstructions reduce variability in homogeneous regions, while preserving discontinuities at region boundaries.

4.4.1. Speckle suppression

We quantify the speckle amplitude in images as described in Sect. 3.2.1, by using the bottom 20 rows (2560 pixels) of the reconstructed images as the clutter region. The results in Table 5 illustrate the speckle suppression achieved by the region-enhanced reconstructions.

Average Associated Peak Distance	T72	BMP2	BTR70
Conventional	3.13 m.	4.32 m.	4.30 m.
Proposed	0.82 m.	1.06 m.	1.25 m.

Table 3. Average associated peak distances in images reconstructed from reduced-resolution (50×50) data.

Average Associated Peak Distance (synthetic T72)	50×50 data	25×25 data
Conventional	1.22 m.	1.35 m.
Proposed	0.07 m.	0.61 m.

Table 4. Average associated peak distances in the synthetic T72 reconstructions.

4.4.2. Segmentation accuracy

We now demonstrate that our region-enhanced images simplify segmentation of the images into target, shadow and background regions. We will use human segmentations of the MSTAR images as the truth. Samples of such human segmentations are shown in the third row of Fig. 9.

We segment our region-enhanced images by simple adaptive thresholding as described in Sect. 3.2.2, using $c_1 = 1.2$ and $c_2 = 2.5$. Sample results of such processing are shown in the bottom row of Fig. 9. These results show that segmentation is considerably simplified by our reconstruction method. If such thresholding-based segmentation were applied to conventional images, the result would be dominated by fluctuations in homogeneous regions.

In Table 6, we present the percentage of accurately classified pixels in our segmentations for the entire data set. We should note that the major error contributing to our results is due to the gap between the target and shadow regions in the segmentations. This is a systematic error and may be improved upon by incorporation of additional information during segmentation. Our error analysis in Table 6 has the limitation that the human segmentations, which we use as the truth, are really not perfect. For example, according to our subjective assessment, the T72 image in the top row of Fig. 9 shows a gun barrel in its shadow. However, the corresponding T72 human segmentation we use, shown in the third row of Fig. 9, does not carry the gun barrel information in the shadow, whereas our segmentation does. This difference contributes to the error of our segmentations in the analysis of Table 6. We should also note that the feature-enhancement parameters λ_1, λ_2, and the thresholding parameters c_1, c_2 have not been optimized for best segmentation performance, but rather picked based on visual assessment of one image, and applied to the processing of the entire data set.

4.4.3. Region histograms

In order to better illustrate the greater class separating property achieved by region-enhanced reconstructions, we show the histograms of the dB-valued reflectivity magnitudes of the target, background, and shadow regions in conventional and region-enhanced T72 reconstructions in Fig. 10. Again, we use the human segmentations to define the true regions. The histograms of different classes for the region-enhanced images appear to be better separated than their counterparts for the conventional images.

5. CONCLUSION

We have demonstrated the feature-enhancement properties of a recently developed regularized SAR image formation method through a variety of quantitative criteria. The results indicate that the images produced by this method exhibit superresolution and improved localization accuracy for dominant scatterers, and improved separability for different regions. With these properties, the method seems to have the potential for improving the performance of ATR systems. Our current work involves running recognition tests on images produced by this technique.

ACKNOWLEDGMENTS

Average Speckle Amplitude	T72	BMP2	BTR70
Conventional	5.919 dB	5.921 dB	5.898 dB
Proposed	2.261 dB	2.283 dB	2.269 dB

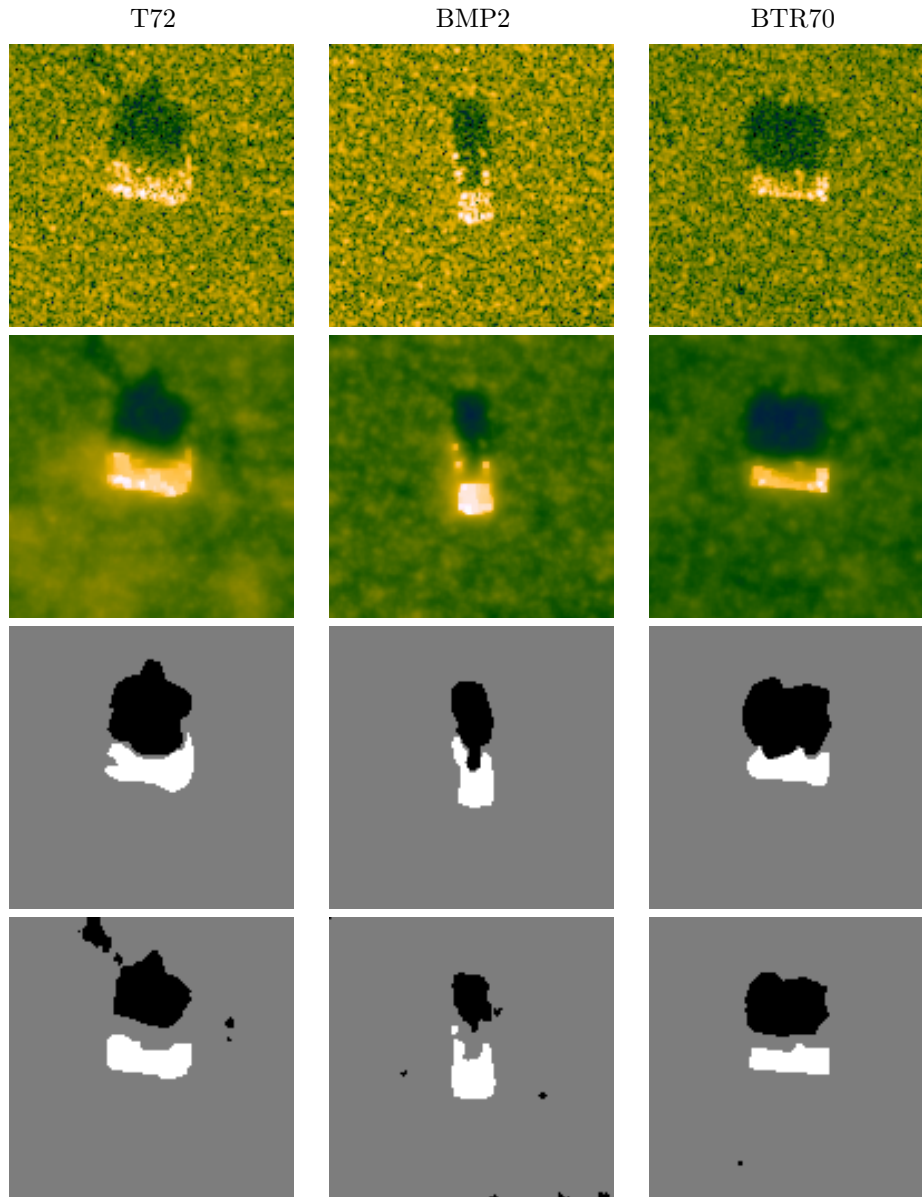**Table 5.** Average speckle amplitude in the dB-valued reconstructed images.

Figure 9. Region-enhanced image formation and segmentation. Top row: MSTAR images. Second row: region-enhanced reconstructions. Third row: human segmentations. Bottom row: threshold-based segmentations of region-enhanced imagery.

REFERENCES

1. J. Walker, "Range-Doppler imaging of rotating objects," *IEEE Trans. Aerosp. Electron. Syst.,* **AES-16**, pp. 23-52, 1980.
2. M. Çetin and W. C. Karl, "Enhanced, high resolution radar imaging based on robust regularization," to appear in *Proc. 2000 IEEE International Conference on Acoustics, Speech, and Signal Processing*, 2000.

	T72	BMP2	BTR70
Average Segmentation Accuracy	96.85 %	97.28 %	97.64 %

Table 6. Average segmentation accuracy measured as the percentage of correctly classified pixels.

Target (conventional)　　　　　Target (region-enhanced)

Background (conventional)　　Background (region-enhanced)

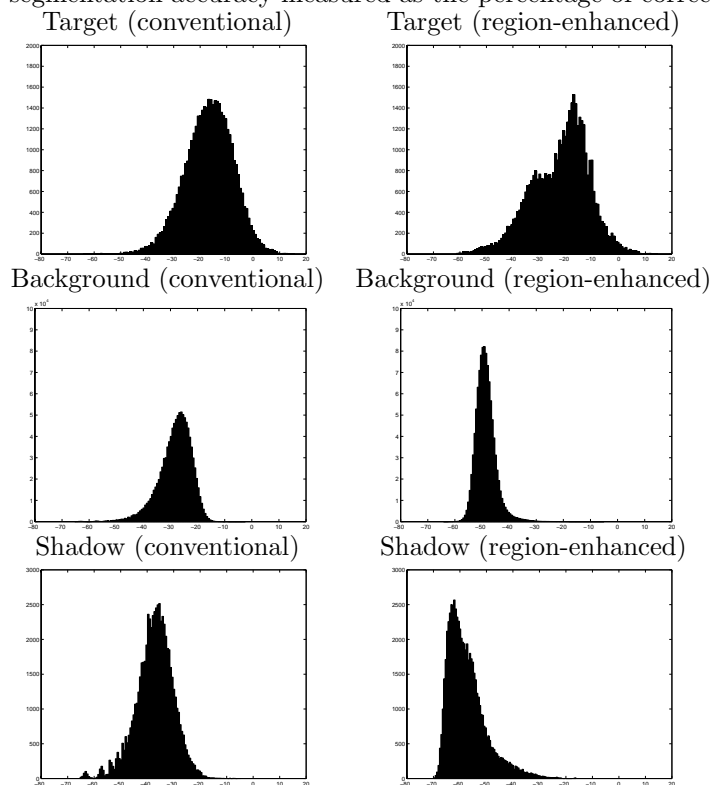Shadow (conventional)　　　　Shadow (region-enhanced)

Figure 10. Histograms of dB-valued reflectivity magnitudes of regions in the T72 reconstructions.

3. L. C. Potter and R. L. Moses, "Attributed scattering centers for SAR ATR," *IEEE Trans. Image Processing,* **6**, pp. 79-91, 1997.

4. G. Jones, III and B. Bhanu, "Recognition of articulated and occluded objects," *IEEE Trans. Pattern Anal. Machine Intell.,* **21**, pp. 603-613, 1999.

5. J. A. Ratches, C. P. Walters, and R. G. Buser, "Aided and automatic target recognition based upon sensory inputs from image forming systems," *IEEE Trans. Pattern Anal. Machine Intell.,* **19**, pp. 1004-1019, 1997.

6. B. Bhanu, "Automatic target recognition: state of the art survey," *IEEE Trans. Aerospace and Electronic Systems,* **AES-22**, pp. 364-379, 1986.

7. A. E. Brito, S. H. Chan, and S. D. Cabrera, "SAR image formation using 2-D re-weighted minimum norm extrapolation," in *Algorithms for Synthetic Aperture Radar Imagery VI,* E. G. Zelnio, ed., *Proc. SPIE,* **3721**, pp. 78-90, 1999.

8. W. Phillips, S. DeGraaf, and R. Chellappa, "Enhanced segmentation of SAR images using non-Fourier imaging," in *Proc. 1998 IEEE International Conference on Image Processing,* **1**, pp. 583-586, 1998.

9. G. R. Benitz, "High-definition vector imaging," *Lincoln Laboratory Journal,* **10**, pp. 147-170, 1997.

10. C. V. Jakowatz Jr., D. E. Wahl, P. H. Eichel, D. C. Ghiglia, and P. A. Thompson, *Spotlight-mode Synthetic Aperture Radar: a Signal Processing Approach,* Kluwer Academic Publishers, Boston, 1996.

11. C. R. Vogel and M. E. Oman, "Fast, robust total variation-based reconstruction of noisy, blurred images," *IEEE Trans. Image Processing,* **7**, pp. 813-824, 1998.

12. D. Geman and G. Reynolds, "Constrained restoration and the recovery of discontinuities," *IEEE Trans. Pattern Anal. Machine Intell.,* **14**, pp. 367-383, 1992.

13. Z. Ying and D. A. Castañon, "Statistical model for occluded object recognition," in *Proc. 1999 IEEE International Conference on Information, Intelligence and Systems,* pp. 324-327, 1999.